Relaxation Effects in Small Critical Flow Venturis

Aaron N. Johnson, Charles. L. Merkle, Michael R. Moldover, and John D. Wright

National Institute of Standards and Technology

100 Bureau Drive, Stop 8361

Gaithersburg, Maryland, 20899-8361, USA

Tel: 301-975-5954, Fax: 301-258-9201, Email: aaron.johnson@nist.gov

ABSTRACT

We computed the flow of four gases (He, N_2, CO_2, and SF_6) through a critical flow venturi (CFV) by augmenting traditional computational fluid dynamics (CFD) with a rate equation that accounts for τ_{relax}, a species-dependent relaxation time that characterizes the equilibration of the vibrational degrees of freedom with the translational and rotational degrees of freedom. Conventional CFD ($\tau_{\text{relax}} = 0$) under-predicts the flow through small CFVs (throat diameter $d = 0.593$ mm) by up to 2.3 % for CO_2 and by up to 1.2 % for SF_6. When we used values of τ_{relax} from the acoustics literature, the augmented CFD under-predicted the flow for SF_6 by only 0.3 %, in the worst case. The augmented predictions for CO_2 were within the scatter of previously published experimental data (± 0.1 %). As expected, both conventional and augmented CFD agree with experiments for He and N_2. Thus, augmented CFD enables one to calibrate a small CFV with one gas (*e.g.,* N_2) and to use these results as a flow standard with other gases (*e.g.*, CO_2) for which reliable values of τ_{relax} and the relaxing heat capacity are available.

A) INTRODUCTION

Critical flow ventruis (CFVs), also called critical nozzles, have been used for decades as secondary standards for measuring large gas flows because they are passive, extraordinarily stable, and easy to use [1, 2]. In an effort to exploit these desirable qualities at the lower flow ranges encountered in semiconductor processing (10 to 300 standard[1] $cm^3\ s^{-1}$), we used computational fluid dynamics (CFD) to

---

[1] Standard reference conditions are at 293.15 K and 101.325 kPa.

predict the flow through a small, well-characterized, CFV (nominal throat diameter d = 0.593 mm[2]). In Figure 1, we compare our CFD results with previously published measurements for four gases [3]. The variables used for this comparison are those conventionally used to describe CFVs. Thus, the ordinate is the discharge coefficient $C_\mathrm{d} \equiv \dot{m}/\dot{m}_\mathrm{i}$, where $\dot{m}$ is actual mass flow and $\dot{m}_\mathrm{i}$ is the mass flow calculated using an idealized one-dimensional, inviscid model. The abscissa is the inverse square-root of the Reynolds number: $\mathrm{Re} = 4\,\dot{m}_\mathrm{i} / \pi\, d\, \mu_\mathrm{o}$ where μ_o is the viscosity evaluated upstream of the CFV at stagnation conditions. As shown in Figure 1, the present CFD model predicts the mass flow through the small CFV for all four gases to within ± 0.31 % for flow rates spanning at least a factor of 4 for each gas. Previously existing CFD models and analytical predictions [4-11] account for several species-dependent effects (virial coefficients and temperature-dependent heat capacity) and for boundary layers and curvature of the sonic line. In order to obtain good agreement with the measurements for CO_2 and SF_6, we had to augment existing equilibrium CFD models to account for τ_relax, the species-dependent relaxation time that characterizes the equilibration of the vibrational degrees of freedom with the translational and rotational degrees of freedom. The relaxation time must be compared to τ_transit, the average time required for a fluid element of fixed mass to move from the CFV inlet to the CFV throat. For any ISO standardized CFV geometry [12] (Figure 2) the approximate transit time is $\tau_\mathrm{transit} \approx 10d/c$ where d is the diameter of the throat and c is the speed of sound in the gas at the CFV throat. Thus, small CFVs, such as the one considered here for use at low flow rates, have short transit times and can encounter larger values of the ratio $\Gamma = \tau_\mathrm{relax} / \tau_\mathrm{transit}$. Conventional CFD and analytical theories for CFVs assume $\tau_\mathrm{relax} = 0$. Such theories agree with the present results for N_2 and He within their scatter (0.1 %, root mean square); however, as shown in the lower panel of Figure 1, conventional theories ($\tau_\mathrm{relax} = 0$) under-predict the flow through this small CFV by up to 2.3 % for CO_2 and up to 1.2 % for SF_6. The augmented CFD model provides better understanding of how gas species effects influence the discharge coefficient for both CO_2 and SF_6 in small CFVs. The results help to quantify the level of correction needed when a CFV is

---

[2] The measured value of the throat diameter was adjusted by less than one micron by matching the experimental C_d data to the computed results for N_2.

calibrated using a standard gas (*e.g.*, N_2 or Air, Ar, etc.) where $\tau_{\text{relax}} = 0$, but applied to other gases (*e.g.*, CO_2 or SF_6) where vibrational relaxation effects are prevalent.

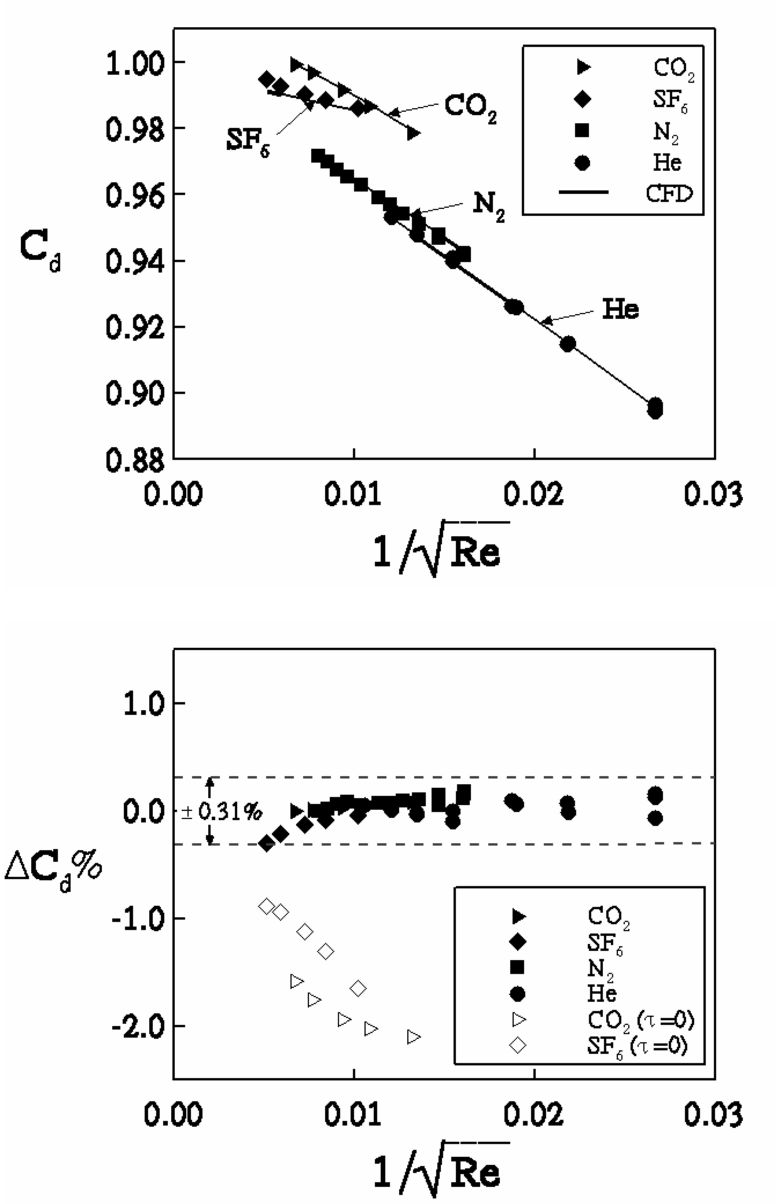

Figure 1: Comparison of experimental calibration data of four gases with equilibrium and non-equilibrium CFD data over a Reynolds number range from 2,000 to 40,000

Our CFD model characterizes the vibrational degrees of freedom within each fluid element by its energy $\varepsilon_{\text{vib}}(T_{\text{vib}})$, where T_{vib} is the vibrational temperature. As the gas flows through the CFV, the temperature of the external modes, T_{ext}, drops quickly while T_{vib} lags behind for molecules where Γ is close to or greater than unity. (Here, we follow Bhatia [13] who called the translational and rotational degrees of freedom "external modes.") To account for the lag, our CFD model couples the Navier-Stokes equations to a local relaxation equation that contains two species-dependent parameters. One is $\varepsilon_{\mathrm{vib}}(T_{\mathrm{vib}})$ which is obtained from spectroscopy [13, 14] and the second is τ_{relax} which is obtained from ultrasonic absorption and dispersion data [15, 16]. The CFD flow field is determined by solving the coupled equations simultaneously.

Our results show that relaxation effects must be considered whenever small CFVs are used for slowly relaxing gases over temperatures ranges for which the vibrational states are significantly populated. Both CO_2 and SF_6 meet these conditions; however, N_2 does not because, at ambient temperature, nearly all N_2 molecules are in their lowest vibrational state.

B) CFV GEOMETRY AND PRINCIPLE OF OPERATION

CFV Geometry

Figure 2 shows the contour of an ISO toroidal throat CFV that was used in this study. It consists of a circular arc of radius $R_c = 2d$ that merges smoothly into a conical section with a vertex half-angle of $\theta = 3^\circ$.

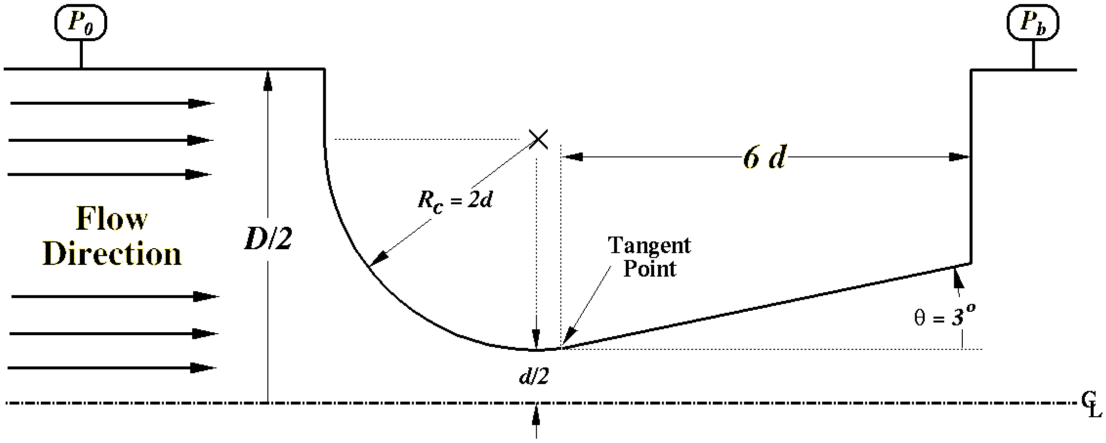

Figure 2: Critical nozzle used in this study. The diameter of the throat was d = 0.593 mm.

Baseline Mass Flow Model

For any CFV, the ratio of the downstream pressure to upstream pressure is maintained so that the gas velocity near the CFV throat reaches sonic velocity. This condition is commonly referred to as choking the

CFV. The largest pressure ratio that just chokes the CFV is called the choking pressure ratio, and CFVs must be operated at or below this threshold. For choked conditions, a long standing *baseline* mass flow model has been developed that is capable of predicting the actual mass flow to within 10 percent or better, depending on Reynolds number. This model is based on the following three assumptions: 1) the flow field is one-dimensional, 2) the flow field is inviscid, and 3) the gas behaves ideally and has constant heat capacities. Herein, these assumptions are collectively called the *baseline CFV assumption*. Several engineering texts [17-19] use this assumption to derive a baseline mass flow

$$\dot{m}_{\mathrm{i}} = \frac{P_{\mathrm{o}}\, A^{*}\, C_{\mathrm{s}}^{\mathrm{i}}}{\sqrt{R T_{\mathrm{o}}}} \tag{1}$$

where P_{o} is the upstream stagnation pressure, T_{o} is the upstream stagnation temperature, $A^{*} = \pi d^{2}/4$ is the CFV throat area, R is the gas constant for a given specie (the universal gas constant divided by the molecular weight), and $C_{\mathrm{s}}^{\mathrm{i}}$ is the ideal critical flow function

$$C_{\mathrm{s}}^{\mathrm{i}} = \sqrt{\gamma}\left(\frac{\gamma+1}{2}\right)^{\left(\frac{1+\gamma}{2(1-\gamma)}\right)} \tag{2}$$

where the superscript "i" is added to denote the gas is ideal and $\gamma = C_P / C_V$ is the ratio of the constant-pressure specific heat to the constant-volume specific heat.

Experimental Calibration

In CFV applications, none of the three assumptions used to derive the baseline mass flow are perfectly satisfied, and consequently the actual CFV mass flow does not equal $\dot{m}_{\mathrm{i}}$. However, the baseline mass flow plays a vital role in CFV calibrations, being used as the normalizing parameter in the definition of the discharge coefficient

$$C_d \equiv \frac{\dot{m}}{\dot{m}_i} = \frac{\dot{m}\sqrt{R T_{\mathrm{o}}}}{P_{\mathrm{o}}\, A^{*}\, C_{\mathrm{s}}^{\mathrm{i}}} \tag{3}$$

where $\dot{m}$ is the experimentally measured mass flow. Calibration curves typically plot the discharge coefficient versus a function of the Reynolds number

$$Re = \frac{4\,\dot{m}_i}{\pi\, d\, \mu_o} \tag{4}$$

where μ_o is the molecular viscosity evaluated at the stagnation conditions.

The C_d values resulting from experimental calibration curves are most reliable when they are applied using the same conditions (*i.e.*, gas species, stagnation conditions, ambient temperature, inlet velocity profile, beta ratio, etc.) for which the CFV was calibrated. This paper focuses on how species effects impact the discharge coefficient when the calibration and application gas differ and one or both of these gases experiences vibrational relaxation. It is important to understand this phenomenon because this physical mechanism is not captured by the standard Reynolds number parameterization. In a similar manner, species effects attributed to real gas behavior (*i.e.*, virial effects) also result in uncoupling between the discharge coefficient and Reynolds number. While the physical mechanisms differ, we introduce linear CFV theory and use it to show that the methodology used to account for real gas behavior can also be applied to correct for vibrational relaxation phenomenon.

In CFV flows, real gas behavior is taken into account by using the real gas critical flow function, $C_{\mathrm{s}}^{\mathrm{r}}$, in the place of the ideal critical flow function, $C_{\mathrm{s}}^{\mathrm{i}}$, in Equation (3). When real gas behavior is accounted for in this way, the corresponding discharge coefficient depends predominately on Reynolds number[3]. In a similar manner, we introduce an *effective* critical flow function, $C_{\mathrm{s}}^{\mathrm{eff}}$, to correct for vibrational relaxation effects. The effectiveness of this correction parameter, like the correction for real gas behavior, depends on vibrational relaxation phenomena being uncoupled from the other higher order effects (*i.e.*, boundary layer development, the shape of the sonic line, and virial effects). Higher order CFV models, which correct the baseline mass flow model, can be used to justify the use of this correction factor.

Higher Order CFV Models

Higher order CFV models improve upon the baseline mass flow model by eliminating the three assumptions used to derive $\dot{m}_i$. These higher order models are based on solutions of the Navier-Stokes

---

[3] Even after correcting for real gas behavior the discharge coefficient has a weak dependence on γ that diminishes with increasing Reynolds number.

equations that govern the fluid dynamics of conventional CFV flows. Because of the complexity of the Navier-Stokes equations, no analytical solutions have been found when all three of the baseline CFV assumptions are eliminated simultaneously. Instead, researchers have found three different solutions by removing only one of the three baseline CFV assumptions while enforcing the other two. These three solutions include 1) a solution to account for the boundary layer development along the CFV wall [6–8], 2) an inviscid axisymmetric solution to account for the curvature of the sonic line at the CFV throat [4], and 3) a solution to account for real gas behavior [20-24]. We briefly discuss each of these three solutions.

In the late 1960's and early 1970's both Tang [6, 7] and Geropp [8] independently developed models predicting how the discharge coefficient is affected by boundary layer development along the CFV wall. The viscous discharge coefficient developed by these researchers

$$C_{\mathrm{d}_1} = f_1\left(Re, \gamma, \mathit{\Omega}\right) \tag{5}$$

is denoted by the subscript "$_1$", and is a function of the Reynolds number, the specific heat ratio, and the CFV geometry which is accounted for via the curvature parameter $\mathit{\Omega} = d/2r_c$ where r_c is the throat radius of curvature. The second model, developed by Hall in 1962, predicts the effects of sonic line curvature on the discharge coefficient. Hall eliminated the one-dimensional assumption by considering the flow to be axisymmetric, but he retained the assumptions that the fluid behaves as perfect gas and the flow is inviscid. The axisysmmetric inviscid discharge coefficient

$$C_{\mathrm{d}_2} = f_2\left(\gamma, \mathit{\Omega}\right) \tag{6}$$

is denoted by the subscript "$_2$", and is a function of the specific heat ratio and the curvature parameter. The third model was developed by Johnson [20-24] who included real gas behavior, but assumed that the flow was inviscid and one-dimensional. This solution requires an accurate thermodynamic database and is typically implemented numerically as described in references [20-24]. For convenience, Johnson expressed the numerically calculated mass flow in the same format as the baseline model

$$\dot{m}_3 = \frac{P_{\mathrm{o}}\, A^{*}\, C_{\mathrm{s}}^{\mathrm{r}}}{\sqrt{R T_{\mathrm{o}}}} \tag{7}$$

and lumped all of the real gas effects into the parameter $C_{\mathrm{s}}^{\mathrm{r}}$, which replaces the ideal critical flow function. The real gas discharge coefficient is denoted by the subscript "$_3$" and defined as the ratio of $\dot{m}_3$ and the baseline mass flow

$$C_{\mathrm{d}_3} \equiv \frac{\dot{m}_3}{\dot{m}_i} = \frac{C_{\mathrm{s}}^{\mathrm{r}}}{C_{\mathrm{s}}^{\mathrm{i}}} \tag{8}$$

but by Equations 1 and 7 is also equal to the ratio of the real gas critical flow function to the ideal critical flow function. The real gas critical flow function, which is often called the *Johnson coefficient*, is generally either tabulated as function of P_{o} and T_{o} or given as a surface fit of these parameters for various gas species.

Linear CFV Theory

For simplicity, in this paper, the three CFV models are referred to as models 1, 2, and 3 respectively. Linear CFV theory is used to combine the individual results of these three models into a single model capable of predicting the discharge coefficient for a general CFV flow where none of the baseline CFV assumptions apply. The results of the linear theory [11] show that to second order accuracy the discharge coefficient equals

$$C_{\mathrm{d}} = C_{\mathrm{d}_1} C_{\mathrm{d}_2} C_{\mathrm{d}_3} \tag{9}$$

the product of the C_{d}'s from models 1, 2 and 3 respectively. This expression clearly shows how the discharge coefficient depends on real gas behavior via C_{d_3}. This dependence can be eliminated by dividing Equation 9 by C_{d_3} , and modifying the discharge coefficient definition to be

$$C_d' \equiv C_{\mathrm{d}} \big/ C_{\mathrm{d}_3} = C_{\mathrm{d}_1} C_{\mathrm{d}_2} \,. \tag{10}$$

Based on the functionality of C_{d_1} and C_{d_2} given in Equations 5 and 6, the modified discharge coefficient is completely free of virial effects, being a function of Re , γ, and Ω . Physically, C_d' is made independent of real gas behavior by using $\dot{m}_3$ as the normalizing parameter

$$C_d^{'} \equiv \frac{\dot{m}}{\dot{m}_3} = \frac{\dot{m}\sqrt{RT_o}}{P_o\, A^*\, C_s^r} . \tag{11}$$

which is equivalent to using the real gas critical flow function in place of the ideal critical flow function. Mathematically, Equation 11 is derived by substituting Equation 3 and 8 into Equation 10.

The definition of the discharge coefficient given in Equation 11 is preferred over the definition in Equation 3 because the real gas behavior in Equation 3 has the undesired quality of possibly permitting the discharge coefficient to be greater than unity. That is, depending on the gas and CFV operating conditions, C_{d_3} could either be greater than or less than unity. In cases where $C_{d_3} > 1$, it could cause the discharge coefficient in Equation 3 to be greater than unity. On the other hand, the definition in Equation 11 is only dependent on boundary layer effects and curvature of the sonic line as shown in Equation 10. Both of these effects cause the discharge coefficient to be less than unity. The boundary layer introduces a region of fluid where both the density and velocity are reduced relative to the core flow. The density is lower because of the higher temperatures in the boundary layer attributed to viscous heating as the flow stagnates at the CFV wall, and the fluid velocity is lower due to the no-slip condition imposed by the wall. In the axisymmetric core flow, the curvature of the sonic line stipulates that the Mach number distribution across the CFV throat cross section is not uniformly equal to unity, but has values both below and above this value. Since compressible flow theory requires that the maximum mass flux coincide with a unity mach number [17], the predicted mass flow will be lower than $\dot{m}_i$.

C) METHODOLOGY

In this section, we present the Navier-Stokes equations that are solved in a conventional equilibrium CFD analysis [9]. We then introduce the extensions required to account for molecular relaxation and we conclude with a description of the numerical algorithms that we used.

Conventional CFD Equations

For Reynolds numbers below 10^6, the axisymmetric, steady, compressible flow in a CFV is governed by the laminar Navier-Stokes equations [9]. The large favorable pressure gradient in the converging section of the CFV is believed to relaminarize what would otherwise be a turbulent flow [25]. Evidence that the flow is laminar is observed in myriads of calibration data where as predicted by laminar flow theory, the discharge coefficient scales linearly with the inverse square-root of the Reynolds number (*e.g.*, Figure 1).

In CFD, the four scalar conservation equations, including continuity, axial and radial momentum, and energy that constitute the axisymmetric Navier-Stokes equations, are often combined into a single vector equation as explained in references [26, 27]. In the present numerical investigation the vector form of the Navier-Stokes equations is expressed as

$$\Upsilon \frac{\partial Q_{\mathrm{v}}}{\partial t} + \frac{\partial E}{\partial x} + \frac{\partial F}{\partial r} = H + \zeta(Q_{\mathrm{v}}) \tag{12}$$

where the time derivative is retained to facilitate a time marching numerical procedure to the desired steady state solution[4]. This vector representation of the Navier-Stokes equations is developed by grouping the appropriate variables from the four scalar conservation equations. In particular, those variables having like derivative operators are combined into vectors. For example, the time derivative vector, $Q_{\mathrm{c}} = [\rho, \rho u_{\mathrm{x}}, \rho u_{\mathrm{r}}, e]^{\mathrm{T}}$, consist of the temporal terms from continuity, axial and radial momentum, and energy equations where $e = \rho[\varepsilon + 1/2(u_{\mathrm{x}}^2 + u_{\mathrm{r}}^2)]$ is the sum of the internal and kinetic energy per unit volume. In Equation 12 the time derivative is multiplied by the Jacobian matrix, $\Upsilon = \partial Q_{\mathrm{c}} / \partial Q_{\mathrm{v}}$, so that via the chain rule of vector calculus [28], $Q_{\mathrm{c}} = [\rho, \rho u_{\mathrm{x}}, \rho u_{\mathrm{r}}, e]^{\mathrm{T}}$, is replaced by $Q_{\mathrm{v}} = [P, u_{\mathrm{x}}, u_{\mathrm{r}}, T]^{\mathrm{T}}$. This transformation to the dependent vector, Q_{v}, conveniently allows thermodynamic properties to be evaluated explicitly as a function of temperature and pressure in the numerical procedure.

The remaining vectors, E and F, on the left hand side of Equation 3 are determined in a manner analogously to Q_{c}. These vectors, commonly called the inviscid flux vectors, are defined as

$$E = \begin{bmatrix} \rho u_{\mathrm{x}} \\ \rho u_{\mathrm{x}}^2 + P \\ \rho u_{\mathrm{x}} u_{\mathrm{r}} \\ (e+P) u_{\mathrm{x}} \end{bmatrix} \qquad F = \begin{bmatrix} \rho u_{\mathrm{r}} \\ \rho u_{\mathrm{r}} u_{\mathrm{x}} \\ \rho u_{\mathrm{r}}^2 + P \\ (e+P) u_{\mathrm{r}} \end{bmatrix} \tag{13}$$

---

[4] The time marching approach differs from commonly used iterative approaches which omit the time derivative term when applied to steady state problems.

and account for the convective terms in the mass, momentum, and energy equations respectively. On the right hand side of Equation 12, the viscous operator, ζ, is defined by

$$\zeta = \frac{\partial}{\partial x}\left(R_{\mathrm{xx}} \frac{\partial}{\partial x} \right) + \frac{\partial}{\partial x}\left(R_{\mathrm{xr}} \frac{\partial}{\partial r} \right) + \frac{\partial}{\partial r}\left(R_{\mathrm{rx}} \frac{\partial}{\partial x} \right) + \frac{\partial}{\partial r}\left(R_{\mathrm{rr}} \frac{\partial}{\partial r} \right) \tag{14}$$

where the viscous matrices, R_{xx}, and R_{xr} are given by

$$R_{\mathrm{xx}} = \begin{bmatrix} 0 & 0 & 0 & 0 \\ 0 & \frac{4}{3}\mu & 0 & 0 \\ 0 & 0 & \mu & 0 \\ 0 & \frac{4}{3}\mu u_{\mathrm{x}} & \mu u_{\mathrm{r}} & \kappa \end{bmatrix} \qquad R_{\mathrm{xr}} = \begin{bmatrix} 0 & 0 & 0 & 0 \\ 0 & 0 & -\frac{2}{3}\mu & 0 \\ 0 & \mu & 0 & 0 \\ 0 & \mu u_{\mathrm{r}} & -\frac{2}{3}\mu u_{\mathrm{r}} & 0 \end{bmatrix} \tag{15}$$

with R_{rx}, and R_{rr} having analogous forms. Finally, the vector H contains the axisymmetric source terms as given in reference [27].

Thermodynamic and Non-Equilibrium Considerations

We follow conventional CFD for dilute gases by computing the density from the equation of state, $\rho = P/[RT(1+B\rho)]$, where the second virial coefficient $B(T)$ accounts for real gas behavior. Data for the second virial coefficient and its temperature derivatives were obtained from references [29, 30]. We used the transport property data as a function temperature (at $P = 101.325$ kPa) from references [31, 32]. In conventional CFD, the equilibrium internal energy $\varepsilon^{\mathrm{eq}}(\rho,T)$ is calculated from a reference state by integrating the ideal-gas constant-volume specific heat $C_{\mathrm{V_i}}$ and subtracting a correction term to account for real gas effects

$$\varepsilon^{\mathrm{eq}}(\rho,T) = \int_{T_{\mathrm{ref}}}^{T} C_{\mathrm{V_i}}\, dT - R\,\rho\, T^2 \frac{dB}{dT} \tag{16}$$

This formula for $\varepsilon^{\mathrm{eq}}(\rho,T)$ is unsatisfactory for the CFV in Figure 2 for certain gases. For this CFV, $\tau_{\mathrm{transit}} \approx 20\mu\mathrm{s}$. Vibrational relaxation times range from $0.0001\mu\mathrm{s}$ to $10\,\mu\mathrm{s}$ depending on gas species, temperature, and density. Thus, the conventional CFD assumption $\Gamma = \tau_{\mathrm{relax}}/\tau_{\mathrm{transit}} = 0$ is a poor approximation for gases with slowly relaxing vibrational modes, especially near the throat of the CFV where the acceleration of the gas is largest. The increase in kinetic energy near the CFV throat is balanced by a decrease in the internal energy of the translational and rotational modes. This reduces the temperature T_{ext} that characterizes these modes. Because the vibrational modes relax slowly, the temperature characterizing them, T_{vib}, is significantly higher than T_{ext}. Consequently, the value of internal energy is not accurately predicted by Equation 16.

To accurately predict the internal energy when $T_{\text{vib}} \neq T_{\text{ext}}$, we sum the relevant molecular components including contributions from translational, rotational, and vibrational modes[5]

$$\varepsilon(\rho, T_{\text{vib}}, T_{\text{ext}}) \equiv \varepsilon_{\text{ext}}(\rho, T_{\text{ext}}) + \varepsilon_{\text{vib}}(T_{\text{vib}}) \tag{17}$$

The second term, $\varepsilon_{\text{vib}}(T_{\text{vib}})$, accounts for the vibrational modes. We assume that the vibrational modes are always in internal equilibrium with each other and we compute $\varepsilon_{\text{vib}}(T_{\text{vib}})$ by summing the contribution of each vibrational mode

$$\varepsilon_{\text{vib}}(T_{\text{vib}}) = \sum_{n=1}^{N} \frac{g_{\text{n}} R \theta_{\text{n}}}{\exp(\theta_{\text{n}} / T_{\text{vib}}) - 1} \tag{18}$$

where g_{n} is the degeneracy for the n^{th} vibrational mode, θ_{n} is the characteristic vibrational temperature for the n^{th} mode, and N is the number of active vibrational modes [13, 14]. The first term in Equation 17, $\varepsilon_{\text{ext}}(\rho, T_{ext})$, is called the *external molecular energy,* which consist of the both the translational and rotational molecular components. Both of these components are taken to be fully equilibrated so that T_{ext} equals the thermodynamic temperature T. The external molecular energy can be defined by subtracting the equilibrium vibrational energy from the equilibrium internal energy

$$\varepsilon_{\text{ext}}(\rho, T_{ext}) = \varepsilon^{\text{eq}}(\rho, T_{ext}) - \varepsilon_{\text{vib}}(T_{ext}) . \tag{19}$$

In this way $\varepsilon_{\text{ext}}(\rho, T_{ext})$ consist only of the translational and rotational components, yet retain real gas behavior that traditional ideal gas models of the translational and rotational components omit.

The exchange of energy between vibrational modes and the combined translational and rotational modes was modeled using the vibrational rate equation [13]

$$\frac{\mathrm{D}\varepsilon_{\mathrm{vib}}(T_{\mathrm{vib}})}{\mathrm{D}t} = \frac{\varepsilon_{\mathrm{vib}}(T_{\mathrm{ext}}) - \varepsilon_{\mathrm{vib}}(T_{\mathrm{vib}})}{\tau_{\mathrm{relax}}} \tag{20}$$

where D/Dt is the time derivative following a fluid element of fixed mass. Bhatia developed this equation for diatomic molecules having only a single vibrational degree of freedom and therefore only one relaxation time [13]. However, Equation 20 works well for polyatomic molecules at temperatures low enough so that only the lowest vibrational degree of freedom is active (*e.g.*, CO_2 near ambient temperature). Often Equation 20 is used to model relaxation in sound and shock propagation through polyatomic gases, such as SF_6, where the highest vibrational modes relax quickly so that the entire heat capacity relaxes at a single relaxation time. However, for certain polyatomic gases (*e.g.*, C_2H_6) more than one relaxation time is needed as discussed by Lambert [33].

For steady flow along a streamline the vibrational rate equation is given by

$$\Gamma \frac{d\varepsilon_{\mathrm{vib}}(T_{\mathrm{vib}})}{dz} = \varepsilon_{\mathrm{vib}}(T_{\mathrm{ext}}) - \varepsilon_{\mathrm{vib}}(T_{\mathrm{vib}}) \tag{21}$$

where $\Gamma = \tau_{\mathrm{relax}} / \tau_{\mathrm{transit}}$ is ratio of the local relaxation time to the local flow transit time, and $z = s/L$ is the normalized distance along a streamline. Here, $\tau_{\mathrm{transit}} = L/\|\vec{u}\|$ is the time that it takes for a fluid particle to move a distance L along a streamline, and $\|\vec{u}\|$ is the magnitude of average velocity over that distance. The relaxation time changes with the local thermodynamic conditions according to the phenomenological Landau and Teller relation [34]

$$\tau_{\mathrm{relax}} = \frac{K_1 \exp\left[(K_2 / T_{ext})^{1/3}\right]}{P} \tag{22}$$

where the constants K_1 and K_2 were obtained by fitting ultrasonic relaxation data [15, 16].

Numerical Solution

The vibrational rate equation and the Navier-Stokes equations must be solved as a coupled system of equations. In this work these equations are solved by globally iterating between the Navier-Stokes equations and the vibrational rate equation until both are simultaneously satisfied. The iterative procedure begins by solving the Navier-Stokes equations with a guessed value of the molecular vibrational energy,

---

[5] The contribution of the electronic energy is negligible over the temperature range of interest.

$\varepsilon_{\mathrm{vib}}(T_{\mathrm{vib}})$. From the latest solution of the Navier-Stokes, the input parameters, $\Gamma = \tau_{\mathrm{relax}} / \tau_{\mathrm{transit}}$ and $\varepsilon_{\mathrm{vib}}(T_{\mathrm{ext}})$, are determined for the vibrational rate equation. Next, the vibrational rate equation is integrated along streamlines to determine the updated vibrational energy, $\varepsilon_{\mathrm{vib}}(T_{\mathrm{vib}})$, which is used to determine the modified internal energy, $\varepsilon(\rho, T_{\mathrm{vib}}, T_{\mathrm{ext}})$, in the next iteration of the Navier-Stokes equations. Consequently, the Navier-Stokes solution and the vibrational rate solution are co-dependent.

Numerical Solution of the Navier-Stokes Equations

The Navier-Stokes equations are solved in a conventional body-fitted coordinate system [35] with a physical domain equivalent to the CFV geometry shown in Figure 2. Grid independent solutions are obtained using a mesh with 201 axial grid points and 101 radial grid points. The axial grid points are uniformly spaced while the radial grid points are spaced exponentially with a higher grid density near the CFV wall to resolve the boundary layer.

An alternating-direction implicit (ADI) numerical algorithm [26, 27] is used for integrating the Navier-Stokes equations. Time advancement is obtained using first-order, backward finite differences. Both inviscid and viscous time-derivative preconditioning [36-38] are employed for accelerated convergence rates over a wide range of Mach numbers and Reynolds numbers. Spatial discretization is accomplished using third order up-winded flux differences for the convective terms and central differences for the diffusive terms. The resulting numerical scheme consists of two tridiagonal matrices that are inverted at each time step using a block version of the Thomas algorithm [26, 27].

In these computations boundary conditions are specified at the CFV inlet, at the CFV exit, along the CFV wall, and on the centerline. At the inlet, the stagnation pressure, stagnation temperature, and flow angle are specified. Characteristic boundary conditions [39] are specified at the supersonic CFV exit. On the CFV centerline, symmetry boundary conditions are used. The CFV wall is taken to be adiabatic with a zero normal pressure gradient, and a no-slip velocity boundary condition.

Numerical Solution of the Vibrational Rate Equation

In contrast to the Navier-Stokes equations, which are expressed in an Eulerian sense, the vibrational rate equation is expressed in a Lagrangian sense. Specifically, the vibrational rate equation describes the rate of relaxation of the vibrational modes of a gas particle of fixed identity moving through the flow field. The Lagrangian paths of particles of fixed identity correspond to streamlines in the flow field. The trajectories of these streamlines must be estimated from the Navier-Stokes solution before the vibrational rate equation can be solved. In the coupling procedure between the two equation sets, the streamlines in the flow field are computed after each time step using the most recent approximation to the Navier-Stokes solution. The vibrational rate equation is then solved on each streamline by a space-marching procedure that integrates between consecutive points on a streamline.

The space-marching procedure begins at the CFV inlet where the vibrational energy on each streamline is equal to its equilibrium value. To find the value of the vibrational energy, $\varepsilon_{\mathrm{vib}}(T_{\mathrm{vib}})$, at the next adjacent grid point along the stream line, the vibrational rate equation is analytically integrated using variation of parameters [40]. In turn, this value of $\varepsilon_{\mathrm{vib}}(T_{\mathrm{vib}})$ serves as an initial condition for the next point, and so on, until the complete streamline has been updated. This process is then repeated for each streamline in the flow field.

D) RESULTS

Validation of CFD Model

The CFD methodology followed the procedure used for the experimental calibration, where the mass flow was controlled by varying the stagnation pressures in the range 50 kPa < P_o < 200 kPa while maintaining the stagnation temperature at 298.15 K. For these operating conditions, the corresponding Reynolds number varied from 1,000 to 40,000 for the small throat ISO standardized CFV. The CFD results were verified by comparisons with experimental data for four gases including He, N_2, SF_6 and CO_2.

The experimental data shown in Figure 1 was obtained by Japan's national flow standard, which measures flow using a gravimetric timed-collection technique with an uncertainty of 0.1 % [3]. As shown in Figure 1, the non-equilibrium CFD model predicted the discharge coefficient to better than 0.3 % for all of the gases over the entire Reynolds number range. In agreement with experimental results, the non-equilibrium CFD model predicted larger C_d values for SF_6 and CO_2 − gases affected by relaxation. As expected, the non-equilibrium CFD model correctly predicted C_{d} for He and N$_2$, gases that are not influenced by vibrational non-equilibrium.

Increase in C_{d} due to Vibrational-Non Equilibrium Flow

When slowly relaxing gases are used in small CFVs, the measured mass flow exceeds the predicted value given by models that assume $\tau_{\mathrm{relax}} = 0$. Indeed, the discharge coefficient as defined in Equation 3 or 11 may even be greater than unity. To understand this phenomenon, it is helpful to consider the limiting cases for the ratio $\Gamma = \tau_{\mathrm{relax}} / \tau_{\mathrm{transit}}$. The limit $\Gamma \to 0$ is the case of equilibrium flow; and the limit $\Gamma \to \infty$ is "frozen" flow in which energy in vibrational modes remains constant. In both limiting cases, the gas dynamic equations are uncoupled from the vibrational rate equation.

In the limit of frozen flow, relaxation does not occur, or, equivalently $\varepsilon_{\mathrm{vib}}(T_{\mathrm{vib}}) = \varepsilon_{\mathrm{vib}}(T_{\mathrm{o}}) = \mathrm{constant}$ throughout the flow field. Because $\varepsilon_{\mathrm{vib}}(T_{\mathrm{o}})$ is constant, the frozen flow heat capacity of the vibrational degrees of freedom are zero ($C_{\mathrm{V_{vib}}} = 0$). Consequently, the specific heat ratio for frozen flow, γ^{fr}, is larger than the equilibrium value, γ^{eq}. The ideal gas model can be used to demonstrate this fact. For an ideal gas, the specific heat ratio is expressible in terms of the translational, rotational, and vibrational heat capacities [18]

$$\gamma_{\mathrm{ideal}} = 1 + \frac{R}{C_{\mathrm{V_{trans}}} + C_{\mathrm{V_{rot}}} + C_{\mathrm{V_{vib}}}} . \tag{23}$$

where γ^{fr} is calculated by setting $C_{\mathrm{V_{vib}}} = 0$. For diatomic or polyatomic gases, having a least one active vibrational mode, $C_{\mathrm{V_{vib}}} > 0$ so that $\gamma^{\mathrm{fr}} > \gamma^{\mathrm{eq}}$.

The increased value of the specific heat ratio in the case of frozen flow results in a higher sound speed in the gas than would exist for equilibrium flow. In addition, as the gas expands and accelerates through the CFV it cools to a lower temperature in the case of frozen flow than it would for equilibrium flow. This lower temperature, subsequently results in a higher density. Both the higher speed of sound and the higher density, in the case of frozen flow, increase the mass flow through the CFV as shown by combining Equations 1 and 2 using the larger frozen flow specific heat ratio in place of normal value of γ. Finally, in the intermediate case of vibrational relaxation, previous CFD results have shown that the mass flow is increased above the equilibrium value, but is less than the frozen flow value [10].

When vibrational relaxation is present, the discharge coefficient as defined by either Equation 3 or 11 is higher than would be predicted by conventional equilibrium models. The larger discharge coefficient results because the normalizing parameter $\dot{m}_\text{i}$ or $\dot{m}_3$ does not account increased mass flow attributed to vibratrional relaxation. Moreover, these definitions allow values of the discharge coefficient that are greater than unity [11]. To avoid this nonphysical situation[6], the discharge coefficient should be defined using a normalizing parameter that accounts for vibrational relaxation effects.

Generalizing the Critical Flow Function to account for vibrational relaxation

Vibrational relaxation can be accounted for by generalizing the critical flow function, which itself is a generalization of the discharge coefficient. Based on linear CFV theory it can be shown that an *effective* critical flow function can be defined as

$$C_\text{s}^\text{eff} \equiv C_\text{s}^\text{r}\left(\frac{C_\text{d}^\text{vib}}{C_\text{d}^\text{eq}}\right) \tag{24}$$

where C_d^vib is the discharge coefficient computed with the present vibrational relaxation flow model, and C_d^eq is the discharge coefficient computed with the equilibrium flow model.

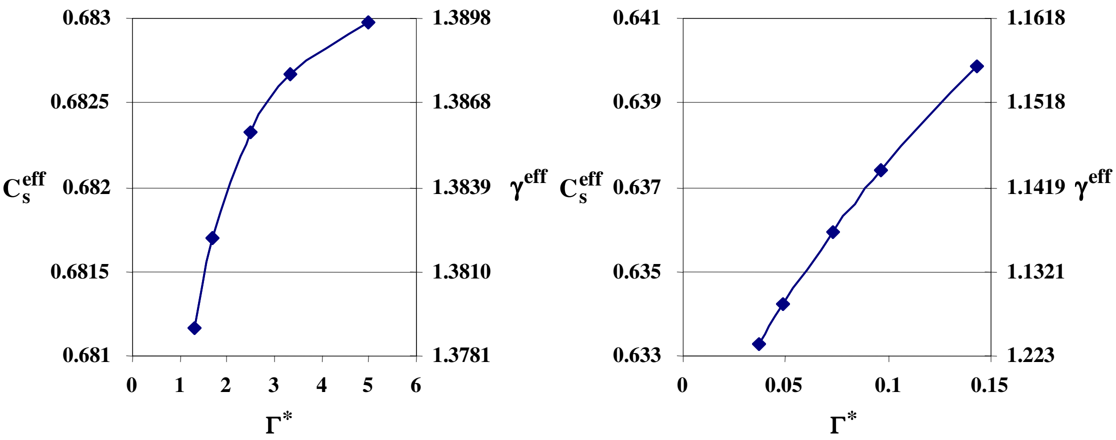

Figure 3: Effective critical flow function versus reference value of Γ* evaluated at the nozzle throat for CO_2 (left) and SF_6 (right).

---

[6] Greater than unity C_d values are sometimes caused by inaccurate values of the CFV throat diameter. This is especially true for small sized CFVs where the throat diameter is more difficult to measure.

Figure 3 shows the *effective* critical flow function for both CO_2 and for SF_6 gases as a function of $\Gamma^*(T_o, P_o) = \tau^*_{\text{relax}} / \tau^*_{\text{transit}}$ where τ^*_{relax} is evaluated at the throat conditions using Equation 22 and $\tau^*_{\text{transit}} = d / c^*$ is the time required for a gas particle to travel one CFV throat diameter at the speed of sound, $c^* = \sqrt{\gamma R T^*}$. The effective critical flow function defined in this way is valid for an ISO standard CFV geometry for T_o near room temperature. For a given gas, C_s^{eff} depends not only on Γ^*, but also on $C_{\text{vib}} / C_v = (\gamma^{\text{fr}} - \gamma^{\text{eq}}) / (\gamma^{\text{fr}} - 1)$, the ratio of the vibrational specific heat to the total constant-volume specific heat. This ratio, which gives an indication of the number of active vibrational modes, is strongly dependent on temperature so that Figure 3 is only valid for T_o near room temperature.

The *effective* critical flow function defines an *effective* specific heat ratio according to the relationship

$$C_s^{\text{eff}} = \sqrt{\gamma^{\text{eff}}} \left(\frac{\gamma^{\text{eff}} + 1}{2} \right)^{\left(\frac{1+\gamma^{\text{eff}}}{2(1-\gamma^{\text{eff}})} \right)} . \tag{25}$$

For both gases CO_2 and for SF_6 the effective specific heat ratio lies between the equilibrium and frozen flow limit, and can be used to assess the degree of vibrational relaxation.

By using C_s^{eff} in the expression for the ideal theoretical mass flow given in Equation 1, the generalized discharge coefficient accounts for vibrational relaxation. The resulting C_d curves for CO_2 and SF_6 will then agree with analytical C_d predictions, having C_d values that are less than unity and that scale with the Reynolds number and the specific heat ratio.

CONCLUSIONS

A model for flow through CFVs that incorporates the influence of the relaxation time of vibrational degrees of freedom has been presented. The model agrees with experimental measurements of the discharge coefficient for four gas species (including CO_2 and SF_6) within 0.31% whereas prior models differed from experiments by as much as 2.3%. The new model couples non-equilibrium thermodynamics with the equations of flow. The pertinent quantities are the energy of vibrational modes and the ratio of the vibrational relaxation time to the transit time for the gas to move from the CFV entrance to its throat. The non-equilibrium phenomena causes an increase in mass flow through the CFV that can be explained by the limiting cases of "frozen" and equilibrium flow. Linear CFV theory is introduced and used to define the appropriate form of the *effective* critical flow function necessary to cancel the effects of vibrational relaxation. The effective values of the specific heat ratio and the critical flow function, presented herein, allow a user to use calibration data performed with N_2 to calculate the flow of CO_2 or SF_6 through a CFV without utilizing the computational model.

ACKNOWLEDGEMENTS

Computational support was provided by the High Performance Systems and Services Division of the Information Technology Laboratory at NIST. In addition, thanks is extended to Nate Briggs for his ideas and support of this work.

REFERENCES

[1] Wright, J. D., “The Long Term Calibration Stability of Critical Flow Nozzles and Laminar Flowmeters,” NCSL Conference Proceedings, Albuquerque, NM., 1998, 443-462.

[2] Wright, P. H., “The Application of Sonic Nozzles to the Automated Accuracy Testing of Gas Flow Meters,” Proc. International Conference on Flow Measurement, Australia 1985, 152-156.

[3] Nakao, S., Hirayama, T., and Takamoto, M., “Effects of Thermalphysical Properties of Gases on the Discharge Coefficients of the Sonic Venturi Nozzle,” Proceedings of the 1997 ASME Fluids Engineering Division Summer Meeting, Vancouver, British Columbia, Canada, June 22-26, 1997.

[4] Hall, I. M., “Transonic Flow in Two-Dimensional and Axially-Symmetric Nozzles,” Quart. J. Mech. and Applied Math, Vol. XV, Pt. 4, 1962, 487-508.

[5] Smith, R. E., Matz, R. J., “A Theoretical Method of Determining Discharge Coefficients for Venturis Operating at Critical Flow Conditions,” Journal of Basic Engineering, 1962, 434-446.

[6] Tang, S. P., “Theoretical Dependence of the Discharge Coefficients of Axisymmetric Nozzles under Critical Flows,” Technical Report PR-118-PU, Department of Mechanical Engineering, Princeton Univ., 1969.

[7] Tang, S., “Discharge Coefficients for Critical Flow Nozzles and Their Dependence on Reynolds Numbers,” Ph.D. Thesis, Princeton Univ., 1969. “””

[8] Geropp, D., “Laminare Grenzschichten In Ebenen Und Rotationssymmetrischen Lavalduesen,” Deutsche Luft- Und Raumfart, Forschungsbericht, pp. 71-90, 1971.

[9] Johnson, A. N., Espina, P. I., Mattingly, G. E., Wright, J. D., Merkle, C. L. “Numerical Characterization of the Discharge Coefficient in Critical Nozzles,” Proceedings of the 1998 NCSL Workshop Symposium, Albuquerque, NM: NCSL 1998.

[10] Johnson, A. N., Wright, J. D., Nakao, S., Merkle, C. L., and Moldover, M. R., "The Effect of Vibrational Relaxation on the Discharge Coefficient of Critical Flow Venturis," Flow Measurement and Instrumentation, 11 (2000), 315-327.

[11] Johnson, A. N., "Numerical Characterization of the Discharge Coefficient in Critical Nozzles", Ph.D. Thesis, The Pennsylvania State University, University Park, PA, 2000.

[12] ISO 9300: (E)., "Measurement of Gas Flow by Means of Critical Flow Venturi Nozzles", Geneva Switz, 1990.

[13] Bhatia A. B., "Ultrasonic Absorption: An Introduction to the Theory of Sound Absorption and Dispersion in Gases, Liquids, and Solids," Oxford University Press, Inc, London W., New York, NY., 1967.

[14] O'Connor, L. C., "Thermal Relaxation of Vibrational States in Sulfur Hexafluoride," The Journal of the Acoustical Society of America, Volume 2, No. 3, January 20, 1954, 361-364.

[15] Estrada-Alexanders, A. F., and Trusler, J. P. M., "Speed of Sound in Carbon Dioxide at Temperatures between (220 and 450) K and Pressures up to 14 MPa," The Journal of Chemical Thermodynamics, Volume 31, No. 5, May 1999, 1589-1601.

[16] Breshears, W. D., and Blair, L. S., "Vibrational Relaxation in Polyatomic Molecules: SF6," The Journal of Chemical Physics, Volume 59, No. 11, December, 1973, 5824-5827.

[17] John, J. E., "Gas Dynamics," Allyn and Bacon, Inc, 2nd edition,} Boston, 1984.

[18] Anderson, J. D. Jr., "Modern Compressible Flow with a Historical Perspective," McGraw-Hill, Inc, New York, 1982.

[19] Shapiro, A. H., "The Dynamics and Thermodynamics of Compressible Fluid Flow," Vol. II, The Ronald Press Co., New York, 1954.

[20] Johnson, R. C., “Calculation of Real-Gas Effects in Flow Through Critical-Flow-Nozzles,” ASME Paper 63-WA-71, 1963.

[21] Johnson, R. C., “Calculations of Real-Gas Effects in Flow Through Critical Nozzles,” Journal of Basic Engineering, September 1964, pp. 519.

[22] Johnson, R. C., “Real-Gas Effects in Critical-Flow-Through Nozzles and Tabulated Thermodynamic Properties,” Nasa Technical Note D-2565, National Aeronautics and Space Administration, Washington, D.C., January 1965.

[23] Johnson, R. C., “Real-Gas Effects in Critical Flow Through Nozzles and Thermodynamic Properties of Nitrogen and Helium at Pressures to 300x105 Newtons Per Square Meter (Approx. 300 atm),” Nasa Technical Note SP-3046, National Aeronautics and Space Administration, Washington, D.C., 1968.

[24] Johnson, R. C., “Real Gas Effects in Flowmetering,” Symposium on Flow, ISA, Pittsburgh, PA, 1971.

[25] White, F. M., “Viscous Fluid Flow,” McGraw-Hill, Inc., 1991.

[26] Hirsch, C., “Numerical Computation of Internal and External Flows: Volume 1, Fundamentals of Numerical Discretization,” John Wiley & Sons, Inc., New York, NY., 1988.

[27] Hirsch, C., “Numerical Computation of Internal and External Flows: Volume 2, Computational Methods for Inviscid and Viscous Flows,” John Wiley & Sons, Inc., New York, NY., 1990.

[28] Davis, D. F., Snider, A. D., “Introduction to Vector Analysis, Sixth Edition,” Wm. C. Brown Publishers, Dubuque, IA., 1991.

[29] Hilsenrath, J., Beckett, C. W., Benedict, W. S., Fano, L., Hoge, H. J., Masi, J. F., Nuttall, R. L., Touloukian, Y. S., Wooley, H. W., “Tables of Thermal Properties of Gases,” U.S. Department of Commerce NBS Circular 564, 1955.

[30] McCarty, R.D. and Arp, V.D., “A New Wide Range Equation of State for Helium,” Adv. Cryo. Eng., 35, 1990, 1465-1475.

[31] Arp, V.D., McCarty, R.D., and Friend, D.G., “Thermophysical Properties of Helium-4 from 0.8 to 1500 K with Pressures to 2000 MPa,” NIST Technical Note 1334, Boulder, CO 1998.

[32] Hands, B.A. and Arp, V.D., “A Correlation of Thermal Conductivity Data for Helium,” Cryogenics, 21(12), 1981, 697-703.

[33] Lambert, J. D., “Vibrational and Rotational Relaxtion in Gases,” Oxford University Press, Wall Street, Oxford, 1977.

[34] Kruger, C.H., Walter G.V., “Introduction to Physical Gas Dynamics,” John Wiley & Sons, Inc., New York, NY., 1965.

[35] Anderson, D. A., Tannehill, J. C., Pletcher, R. H., “Computational Fluid Mechanics and Heat Transfer,” Hemisphere Publishing Corporation, New York, NY., 1984.

[36] Buelow, P., Venkateswaran, S., and Merkle, C. L., “The Effect of Grid Aspect Ratio on Convergence,” AIAA Journal, Vol. 32, 1994, 2401-2406.

[37] Feng, J., and Merkle, C. L., “Evaluation of Preconditioning Methods for Time Marching Systems,” AIAA Paper 90-0016, AIAA 28th Aerospace Sciences Meeting, Reno, NV. 1990.

[38] Buelow, P. E. O., “Convergence Enhancement of Euler and Navier-Stokes Algorithms,” PhD thesis, Department of Mechanical Engineering, 1995, The Pennsylvania State University, University Park, PA.

[39] DuChateau, P., and Zachmann, D., “Applied Partial Differential Equations,” Harper and Row Publishers, Inc. 1989.

[40] Edwards, C. H., and Penny, D. E., “Elementary Differential Equations With Boundary Value Problems,” Prentice-Hall, Inc., Englewood, NJ., 1989.